Universiteit
Leiden
The Netherlands

# UV Photodesorption and photoconversion of interstellar ices: the laboratory perspective

Bulak, M.

**Citation**
Bulak, M. (2021, December 9). *UV Photodesorption and photoconversion of interstellar ices: the laboratory perspective*. Retrieved from https://hdl.handle.net/1887/3245781

| | |
|---|---|
| Version: | Publisher's Version |
| License: | Licence agreement concerning inclusion of doctoral thesis in the Institutional Repository of the University of Leiden |
| Downloaded from: | https://hdl.handle.net/1887/3245781 |

**Note:** To cite this publication please use the final published version (if applicable).

# 2 | MATRI$^2$CES


## Abstract

Interstellar ices have a profound impact on the physical and chemical processes during star and planet formation sequence. In an experimental setup, MATRI$^2$CES (Mass Analytical Tool to study Reactions in Interstellar ICES), ice analogues are synthesized and irradiated with vacuum-ultraviolet photons at low temperature (20 K). The photochemical evolution of the ice is quantitatively traced with a combination between laser-desorption and time-of-flight mass spectrometry, a toolbox unique for astrochemistry. In this chapter, a detailed description of the setup is provided, including an experimental upgrade, which resulted in a current detection limit of $3 \times 10^{11}$ molecules cm$^{-2}$. The key calibration procedures are demonstrated, followed by a step-by-step analysis of the resulting data. MATRI$^2$CES offers a sensitive experimental tool, complementary to more common techniques like RAIRS and TPD-QMS, which is applied to investigate the solid-state origin of species, including complex organic molecules. In addition, it is used to accurately determine the UV photodesorption rates of interstellar ices, important for the balance between ice and gas in cold regions representing various stages of star and planet formation.



Bulak, M., Paardekooper, D.M., Fedoseev, G., Samarth, P., Bouwman, J., Chuang, K-.J., Linnartz, H., Rev. Sci. Instrum., in preparation

## 2.1 Introduction

In this chapter, a description of the experimental setup used for this thesis is provided. MATRI$^2$CES (Fig. 2.1), the Mass Analytical Tool to study Reactions in Interstellar ICES, is an apparatus designed to simulate the interstellar ices in different regions of the ISM. The system in its original form was built in 2013 (Isokoski 2013) and upgraded over the last years to gain sensitivity and allow more sophisticated ice chemistry experiments, with details described in Paardekooper et al. (2014) and Bulak et al. (in prep). The basic concept of this setup differs from those applied in ice setups used elsewhere and allows to combine laser desorption and time-of-flight mass spectrometry, resulting in an *in-situ* probing technique that allows quantitative analysis of photon-triggered processes in ices. The fundamental principle and approaches of the different types of measurements with MATRI$^2$CES, as well details of the data analysis are provided in the next sections.

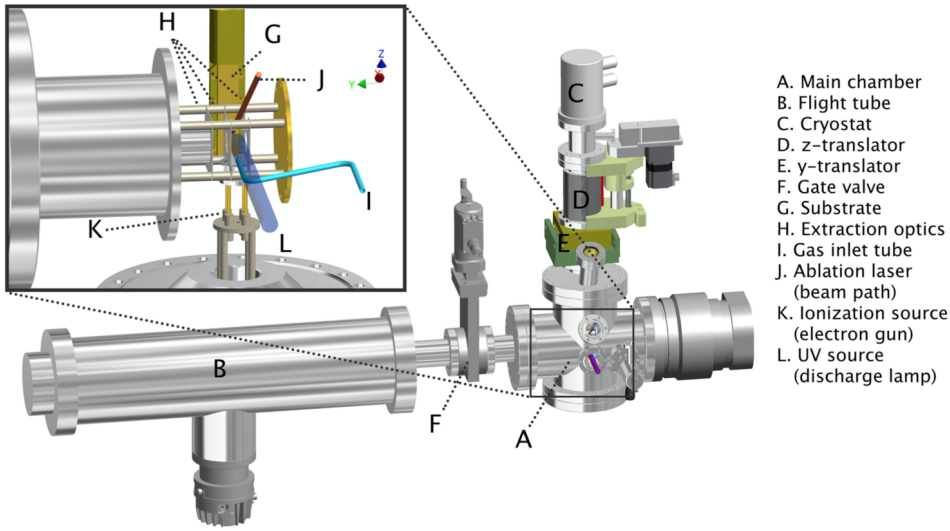


**Figure 2.1:** A schematic view of the experimental setup MATRI$^2$CES used in this thesis. Figure is adapted from Paardekooper et al. (2014)

## 2.2 System description

A schematic 3D view of the experimental system MATRI$^2$CES is shown in figure 2.1 along with its main components. The system consists of two vacuum chambers: the main chamber (A in Fig. 2.1) and the time-of-flight mass spectrometer tube (B, Jordan TOF products, Inc.), both at a base pressure of $\sim 10^{-10}$ mbar (equivalent to $\sim 10^6$ particles cm$^{-3}$). The main chamber houses a closed-cycle helium cryostat (C, Advanced Research System, DE 202), which cools down a gold-coated copper block, used as a substrate for ice deposition (G). The temperature of the substrate is controlled between 20-300 K, through resistive heating of the copper block that is continuously cooled by the cryostat, using a temperature controller (Lakeshore 331). Temperature

values are measured using chromel-gold/iron alloy thermocouples with an absolute accuracy of ±1 K. The cryostat is mounted on top of two translation stages (D, E), allowing a linear shift in the position of the substrate in two dimensions (y- and z-directions). The translation along the z-direction (50 mm) is motorised, allowing to control the vertical motion of the substrate with variable speeds. The position of the substrate in the y-direction is adjusted manually (15 mm). The ices are deposited under fully controlled conditions via an inlet gas tube (I), connected to a gas manifold, with a base pressure in the range of $\sim 10^{-4}$ mbar. The ice deposition rate is calibrated using He-Ne laser interference measurements (Section 2.3.1).

The spectral energy distribution (SED) of the interstellar radiation field includes Lyman-$\alpha$ (121 nm), a molecular $H_2$ emission (130 - 165 nm), and can be closely simulated by a microwave discharge $H_2$ lamp (MDHL). The MDHL is connected to the main chamber via a magnesium fluoride viewport, opposite from the substrate, at a distance of 14 cm (L). The lamp (borosilicate) has a F-type design with an Evenson cavity placed on it, characterized in detail by Ligterink et al. (2015). The $H_2$ plasma is powered by a microwave generator (Sairem, 2.45 GHz, 80 Watts) and the lamp is operated with a continuous flow of $H_2$ gas maintaining a pressure of 1.4 mbar. The calibration of the resulting VUV photon flux is key in accurately describing the photon-triggered process, hence the calibration procedure is described in separately in Section 2.3.2.

The probing of the ice composition is initiated by laser ablation of a small spot (diameter of ∼1 mm) on the deposited ice with an unfocused laser beam of a Nd:YAG laser (J, Polaris II, New Wave Research, 3-4 nanoseconds). The energy of the laser pulse (typically between 10 and 55 mJ $cm^{-2}$) is calibrated for each species and ice thickness to be sufficient for complete desorption of the ablated spot. This results in a gas phase plume of species with a net velocity vector away from the substrate (x-direction). The travelling plume is ionized via dissociative electron impact ionization (electron gun, K). The continuous electron beam is guided along the z-axis in the near vicinity of the substrate, and has an average electron energy of 70 eV. The involved electrons do not interact with the ice substrate. The average electron energy corresponds to the highest electron ionization cross sections for most species, resulting in a maximized ion formation efficiency. The ionization event also induces fragmentation of the species, which offers an additional tool to guide unambiguous identification (if the fragmentation pattern is available). In the case of overlapping mass fragments from multiple molecules, the mass analysis is complicated. It is possible to (partially) overcome this issue by using lower electron energies (i.e., 20 eV) that come with less fragmentation and moreover different fragment intensities, as well as the explicit use of isotopically enriched precursor species.

Ions are generated within the ion extraction optics (H) - metal plates oriented orthogonally to the substrate, each carrying a voltage of 1050 V. After a preset time delay (Fig. 2.2) following the laser shot, a fast (4 $\mu$s) decrease in the voltage (by 100 V) on one of the plates results in an extraction of the ions towards the electric-field-free time-of-flight tube (81.28 cm). Before entering the tube, the ions are gently steered along the x-direction in order to guide them towards the detector, which is off-center. This is done via a constant potential difference (100 V) applied to $V_x$ plates in Fig. 2.3. During the drift in the time-of-flight tube, ions are separated according to their mass over charge ratio (m/z). Lower masses arrive earlier than heavier masses and this time resolution allows to record mass selective signals. To improve the mass resolution of

our spectra, the TOF MS is operated in a reflectron mode. This means that at the end of the time-of-flight tube, ions are reflected back, allowing to minimize the effect of variations in the initial kinetic energy within the plume. The detector is a 40 mm microchannel plate (MCP), with a high electric field applied across its plates (2400 - 3000 V). This allows a single ion to trigger an electron cascade, with the signal gain regulated by the MCP voltage. For each ion (m/z) a time-of-flight between the extraction optics and the MCP detector is recorded with a Data Acquisition card (DAQ) at a sampling rate of 2.5 GHz and used to ultimately derive the composition of the probed ice.

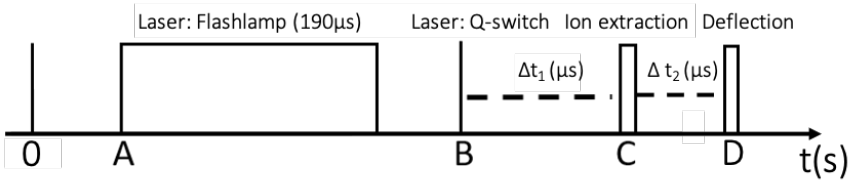


**Figure 2.2:** Relative timing sequence of LDPI TOF MS technique including the laser shot (A, B) and ion extraction (C) into the TOF MS. The time delay of the ion extraction ($t = B + \Delta t_1$) is varied in order to optimize detection settings for a particular product or probe the complete distribution of the plume. The timing of deflection ($t = C + \Delta t_2$) is relevant only for the last section of this chapter.

The timing of the LDPI TOF MS probing sequence (laser shot, ion extraction, data acquisition) is shown in Fig. 2.2. It is controlled with a time/delay generator (DG 535, Stanford Research System), which is triggered 100 times at a frequency of 5 Hz. This is synchronized with the vertical motion of the substrate (z-direction) allowing each laser shot to probe a 'fresh' spot along a column of the ice. To probe the changes in the ice composition and thickness as a function of UV radiation dose, the substrate is shifted along the y-axis and a fresh column of ice is probed (9 non-overlapping columns). The recorded 100 spectra are averaged (at the same timing sequence), to improve the signal to noise ratio, and used for further analysis. Alternatively, the time delay ($\Delta t_1$) can be varied every 10 spectra, to collect a complete distribution of the plume profile.

### 2.2.1 Limit of detection

The sensitivity of MATRI$^2$CES to detect low abundances of photoproducts has been limited by the dynamic range of the MCP. The amount of signal generated by the parent species (typically a molecular ion) causes saturation of the detector at the voltages of 2500 V across the MCP detector. A repeated saturation of the detector (signal above 1 V) leads to damage, hence the MCP has been operated at relatively insensitive settings. A solution has been implemented to utilize the full potential of the system. A high voltage pulser with a nanosecond rise time was added to the setup and connected to the $V_x$ plates in Fig. 2.3. A short voltage pulse (0.2 - 5$\mu$s) is applied to the ion optics at a precisely calibrated delay ($t = B + \Delta t_2$) to deflect the most abundant ions (minimum deflected range of 3 - 5 atomic mass units). This prevents

the most abundant species from reaching the detection, i.e. to go into saturation, and allows to increase the gain across the MCP, successfully lowering the limit of detection (LoD) in other parts of the mass spectrum (Section 2.5).

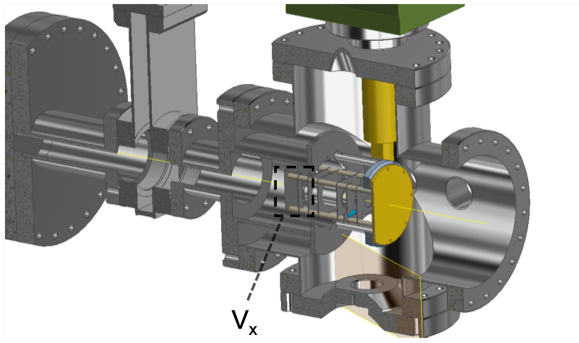


**Figure 2.3:** A short voltage applied to the $V_X$ metal plate (duration of 0.2 - 5$\mu$s, 50 V) is timed to deflect the most abundant ions, ultimately to increase the sensitivity (improving the detection limit) on MATRI$^2$CES.

## 2.3 Calibration measurements

### 2.3.1 Ice thickness

An all-metal high-precision leak valve controls the ice deposition rate. It connects the gas manifold used for sample preparation with a gas tube in the main chamber, under an angle of 85° with respect to the substrate. Laser interference measurements are used to calibrate the ice deposition rate (Hudgins et al. 1993). During an ice growth, a He-Ne laser beam (wavelength 632.8 nm) is reflected from the substrate at an incident angle of 3°($\theta$). The reflected light is collected with a photodiode (Thorlabs PDA36A) and its intensity is recorded with an oscilloscope as a function of time. Figure 2.4 shows data collected for a deposition of CO ice at 20 K with a preset needle valve setting (15) and CO pressure in the gas manifold equal to 40 mbar. The resulting interference pattern of subsequent minima and maxima can be used to derive the ice deposition rate ($\tau$). First, the ice thickness (d) is described as a function of the number of interference fringes (m) as in equation 6.2:

$$d = \frac{m \cdot \lambda}{2 \cdot \frac{n_1}{n_0} \cdot \cos\theta}, \tag{2.1}$$

where $\lambda$ is 632.8 nm, $n_0$ and $n_1$ are refractive indices of the vacuum (1) and ice, and $\theta$ is the angle of refraction (3°). The ice growth rate (in mol. cm$^{-2}$s$^{-1}$) can be determined from:

$$\tau = \frac{d \cdot \rho \cdot N_{\mathrm{A}}}{M \cdot t}, \tag{2.2}$$

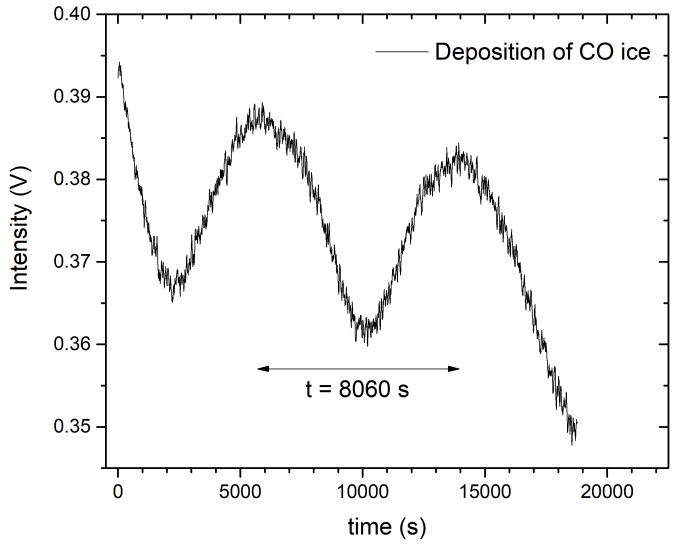


**Figure 2.4:** An interference pattern recorded during the CO growth at 20 K. The overall loss in the intensity is caused by scattering of the light in the ice, which does not affect the interference period.

where t is the time corresponding to the thickness d (calculated using equation 6.2), $N_A$ is Avogadro's number ($6.022 \times 10^{23}$ mole$^{-1}$), $\rho$ is the ice density in (g cm$^{-3}$), and M is the molar mass of the species (in g mole$^{-1}$). To calculate the CO ice deposition rate, the following values are used: molar mass of 28 g mole$^{-1}$, ice density equal to 0.8 g cm$^{-3}$, $n_1$ equal to 1.27 and the period for one fringe of 8060 s (Roux et al. 1980). These values are plugged into Eq. 2.2 and result in an ice deposition rate of $5.3 \times 10^{13}$ molecules cm$^{-2}$s$^{-1}$. A deposition of a typical ice thickness of 20 monolayers (1 ML = $1 \times 10^{15}$ molecules cm$^{-2}$) takes around 6 minutes.

### 2.3.2 Microwave discharge hydrogen lamp

The VUV photon flux of the MDHL used in our experiments has been determined at the position of the substrate, with a 1 cm$^2$ NIST-calibrated AXUV-100 photodiode. The photocurrent corresponding to the amount of radiation on the photodiode is measured with a Keithley 485 picoammeter. To separate the contribution of the photons in the visible range, a second MDHL lamp has been operated at the identical conditions, with a seal (fused silica) that transmits in the visible range with 90% efficiency and absorbs photons in the VUV ($\lambda < 230$ nm). The difference between the two measurements (MDHL sealed and not sealed) allows to subtract the photocurrent linked to visible photons, and to derive the VUV photon flux (F($\lambda$)) using equation 2.3:

$$F(\lambda) = \frac{i(\lambda}{e \cdot \epsilon(\lambda)}, \tag{2.3}$$

where $i(\lambda)$ is the VUV photocurrent (Ampere), $e$ is the electron charge ($1.6 \times 10^{-19}$ C) and $\epsilon(\lambda)$ is the number of electrons per absorbed photon of the NIST photodiode (quantum efficiency). The SED of the lamp at the operating conditions has been measured for a large number of different settings in (Ligterink et al. 2015). The derived VUV photon flux based for the conditions applied in this thesis research project is $(2.5 \pm 0.5) \times 10^{14}$ photons $cm^{-2}s^{-1}$.

## 2.4 Data analysis

The analysis of the LDPI TOF MS spectra consists of three steps: mass calibration, integration of the area under the mass peaks, and conversion of the calculated signal into a column density of identified species. The first step in the data analysis is the mass calibration of the time-of-flight spectra. This is done via a two-point calibration, where two known ions (m/z based on the initial composition of the ice) are used to solve the conventional equation of the time-of-flight (TOF):

$$TOF = A + B \cdot \sqrt{m/z}, \tag{2.4}$$

An example of a mass calibrated spectrum of $H_2O$ ice acquired via LDPI TOF MS is shown in Figure 2.5. The thickness of the ice is 100 ML, following the ice deposition rate calibration described in Section 2.3.1. The mass resolution of the peaks calculated with M/ΔM 300. Here gives M the m/z value and ΔM is the full width half maximum of the peak. The mass peaks at m/z = 16, 17, 18 represent fragments of $H_2O$ created upon electron impact ionization, in agreement with the NIST database (Kim et al. 2014). In addition, peaks at m/z = 18·n+1, where n = 1, 2 represent protonated water clusters formed upon laser desorption of water ice; these species are not formed upon VUV irradiation and do not influence the ongoing ice chemistry (Gudipati & Yang 2012). The intensities of the mass peaks (integrated area) are proportional to a linear combination of species present in the plume (Paardekooper et al. 2014). This allows to express an integrated mass spectrum, $M_t$, at a given irradiation time, t, by:

$$M_t = \sum_{i=1}^{n} a_i \cdot \sigma_i \cdot M_i, \tag{2.5}$$

where $a_i$ is the molecular abundance of species i, $\sigma_i$ is the electron impact ionization cross section (at 70 eV), and $M_i$ is the corresponding fragmentation fraction. The area under each mass peak is calculated by fitting a Pearson IV distribution, which provides an excellent fit to the data by taking into account the asymmetry of the peaks and "spikiness" (Pearson 1895; Castellanos et al. 2018). An example of a fit is given by Fig. 2.6. The error associated with the fit is estimated by calculating the root mean square over the residual within one standard deviation from the center. The sum of the integrated area of the mass peaks between m/z = 16 and 18, is linked with the column density of water ice via Equation 2.5. After taking into account the ionization cross-section for water (2.275 $Å^2$, Kim et al. 2014), the resulting value is set equal to 100 ML of water ice or $1 \times 10^{17}$ molecules $cm^{-2}$. This value is then used as a reference to calculate the photodepletion of the parent or formation of photoproducts, after taking into account the fragmentation pattern and ionization cross-section. For

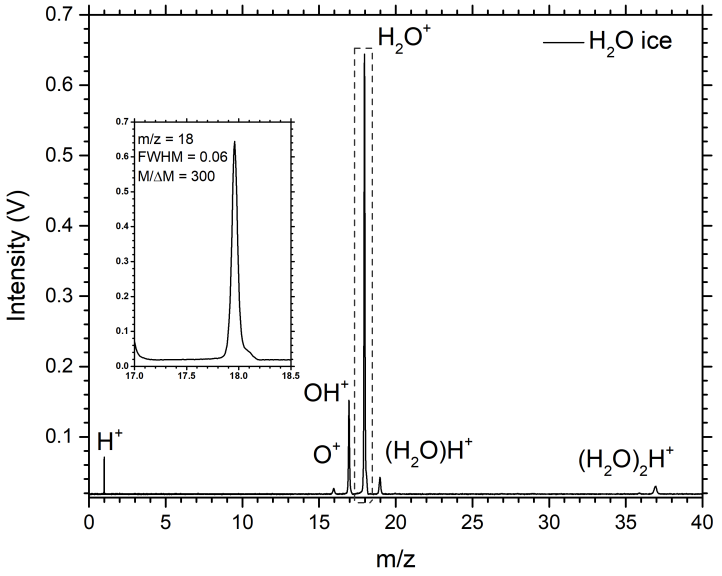


**Figure 2.5:** LDPI TOF MS of $H_2O$ ice deposited at 20 K. The ice thickness in 100 ML. The inset shows the mass signal corresponding with $H_2O^+$ ion at m/z = 18, to demonstrate the mass resolution of the spectra.

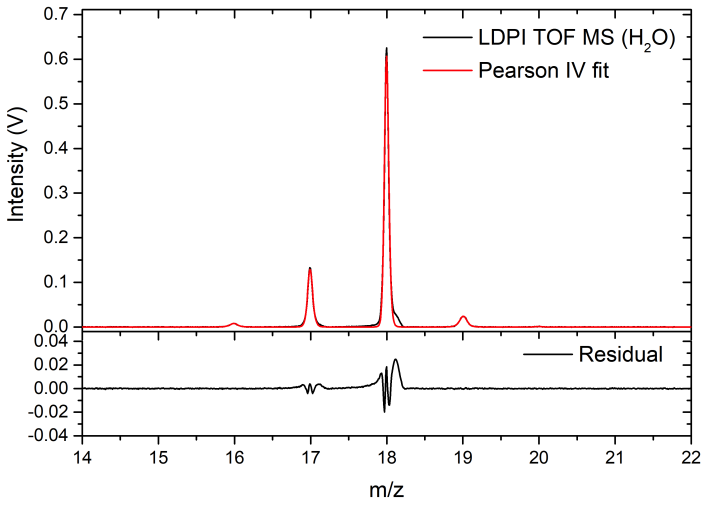


**Figure 2.6:** A Pearson IV fit to the LDPI TOF MS. The lower panel shows the residual to the corresponding fit.

example, for photoformation of $O_2$, the molecular ion at m/z = 32) is integrated, however a part of its fragmentation pattern overlaps with a water fragment (m/z = 16), preventing from clearly disentangling the contribution of each molecules. This is solved by considering the fragmentation pattern available at NIST, with 22% of $O_2$ residing in the fragment of m/z = 16 (Kim et al. 2014). After including the ionization cross section of $O_2$ (2.441 Å$^2$), the resulting value is converted with respect to the initial column density of water, allowing to trace its formation as a function of VUV fluence. A further option to circumvent overlapping masses is to work with isotopically enriched species, as will be shown later in this thesis for several experiments.

## 2.5 Measuring toolbox

This section focuses on the different types of measurement/data analysis methodologies performed with MATRI$^2$CES, as these provide the basis for quantifying the impact of a photon-triggered process. The most valuable is the capacity to measure the chemical kinetics at low ice temperature. The second concerns the identification of formed photoproducts using Temperature Programmed Desorption. The third topic deals with an improvement in the limit of detection on MATRI$^2$CES.

### 2.5.1 VUV photolysis at 20 K

The LDPI TOF MS traces of $CH_3CN$ ice upon VUV photolysis at 20 K are collected; already for a small dose of VUV photon fluence, a multitude of new features appears in the spectra. The assignment of these mass peaks to particular products is a multi-

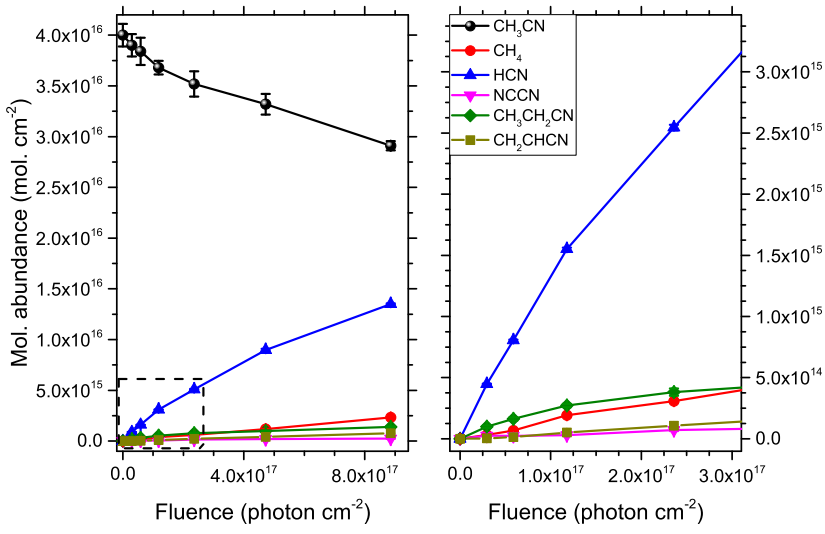


**Figure 2.7:** *Left panel:* Molecular abundances of species during the UV photolysis of $CH_3CN$ ice as function of photon fluence. *Right panel:* Zoom in of the low fluence region indicated in the left panel.

step process, which begins with considering the radical species which are formed upon VUV photodissociation. The recombination of radicals typically dominates the photoconversion, however, radical-neutral interactions can also play a role. In this case, two of the products can be immediately suggested: $CH_4$ ($CH_3$+H) and HCN (CN+H). Indeed their mass spectral signatures fit the collected LDPI TOF MS. Experiments with a deuterated acetonitrile ($CD_3CN$) confirm these assignments. In these experiments, the observed mass peak shifts correspond to the substitution of HCN (m/z = 27) → DCN (m/z = 28) and $CH_4$ (m/z = 16) → $CD_4$ (m/z = 20). The data analysis is performed as described in Section 2.4 and as a result, chemical kinetics of the parent species and photoproducts derived at 20 K, are shown in Fig. 2.7. The demonstrated photodepletion of the parent species is a combined effect of photoconversion and photodesorption. To separate these two processes, an experiment with a UV-transparent Argon cap is performed, which literally blocks the photodesorption, but has a minimum effect on the photoconversion (Chapters 3 and 5).

### 2.5.2 Temperature Programmed Desorption with TOF MS

In typical temperature programmed desorption, species desorb from the ice at characteristic temperatures, which provides a complimentary tool for product identification. On MATRI$^2$CES, the typical TPD is only possible for temperatures above the sublimation threshold of the parent species. This is due to a risk related to operating high voltages at a high pressure (up to $10^{-6}$ mbar upon the thermal desorption of the parent), which can cause an electrical spark with devastating effects on the electronics of MATRI$^2$CES. An alternative is a comparison of mass peak intensities collected via LDPI TOF MS at different temperatures, allowing for stabilizing the temperature of the substrate and the pressure in the chamber, prior to turning on the high voltages. As an example, following a VUV irradiation of $CH_3CN$ at 20 K, the ice is probed with LDPI TOF-MS in specific temperature ranges, typically above and below the desorption temperature of an abundantly formed photoproduct. As a result, an intensity decrease of characteristic mass peaks is observed. This process can be explained by the thermal desorption of a photoproduct. This is demonstrated for $CH_4$ and HCN in Fig. 2.8. A comparison between mass spectra at 60 K and 130 K shows a decrease in the mass peak at m/z = 27, which is a characteristic peak of HCN, expected to desorb around 120 K. In addition, thermal desorption of remaining $CH_4$ trapped in the ice is observed at m/z = 16. The integrated (difference) mass spectra demonstrate the thermal desorption of $CH_4$ and HCN at expected temperatures and can be used as a supplementary identification tool.

Classical temperature programmed desorption has been performed on MATRI$^2$CES for the first time, following VUV photolysis of $CH_3CN$ and starting at a temperature above the sublimation threshold of $CH_3CN$, around 150 K. The data acqusition sequence, without the laser, can be run at a much higher frequency (500 Hz). This results in an improvement in the signal to noise of the data. The substrate is heated at a rate of 2 K/minute and the species recorded with the TOF have been binned into 30 K intervals, shown in Fig. 2.9. The identification of photoproducts in Chapter 5 has been cut off at the second generation of products (m/z of around 80), due to uncertainties related to their identification. Despite that, the figure shows the incredible chemical complexity that can form upon VUV photolysis of $CH_3CN$, with the largest species consisting of 10 atoms (C/N/O). Identifying the typical fragmentation

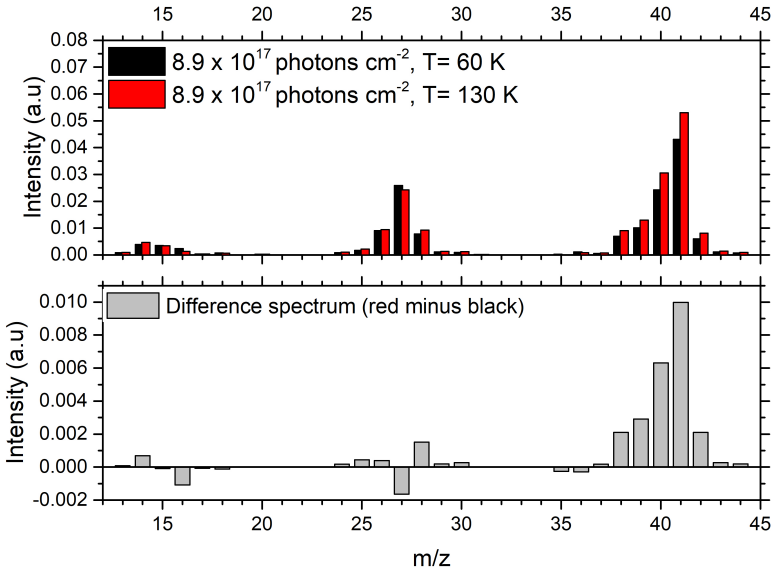


**Figure 2.8:** Top panel: integrated LDPI TOF-MS signals for an UV-irradiated $CH_3CN$ ice at 20 K that is subsequently heated to a temperature of 60 K (black sticks) and 130 K (red sticks). The identification of HCN formation in the ice becomes visible when subtracting the 130 K and 60 K data as HCN thermally desorbs around 120 K. This is shown in the lower panel; at m/z = 27 this results in a negative value. In addition, thermal desorption of remaining $CH_4$ trapped in the ice is observed at m/z = 16.

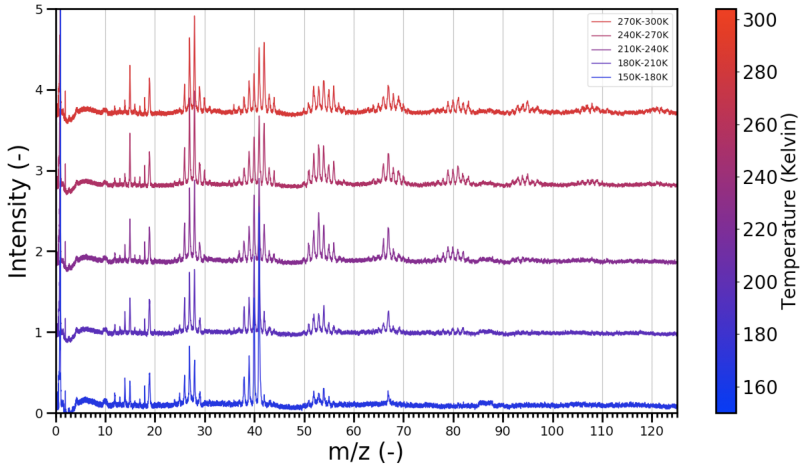


**Figure 2.9:** TPD TOF MS between 150 K - 300 K following a VUV photolysis of the $CH_3CN$ ice. The mass spectra collected continuously during the heating up of the substrate, without the use of LDPI.

patterns of different families of species (amides, nitriles, carboxylic acids, etc.) is the next step in interpretation of this rich dataset.

### 2.5.3 Increasing the detection sensitivity

Finally, the most recent development on the setup has been an addition of a high voltage pulser, calibrated to deflect the ions that typically saturate the MCP detector (see Fig. 2.3). To test the limit of detection before and after the implementation of the pulser, we designed a scheme, in which the $3\sigma$ detection can be described in terms of detected ice column density (molecules per $cm^2$). An argon ice is deposited at 20 K with column density of 17.5 ML. Argon has been chosen as it has three natural isotopes with masses 36, 38, and 40 at low natural abundances of 0.334%, 0.063%, and 99.604%, respectively. With the 'old' settings, the $^{36}Ar$ peak is clearly detected with the S/N of $7\sigma$ (MCP of 2520 V), where the S/N is calculated by dividing the absolute intensity of the feature by standard deviation of the noise level in the spectrum, see Fig. 2.10. The $7\sigma$ detection corresponds to $1.4 \times 10^{13}$ mol.cm$^{-2}$, hence the LoD at $3\sigma$ is $6 \times 10^{12}$ mol.cm$^{-2}$. This trace is labeled 'Pulser OFF'. It is important to note that at the used MCP value of 2520 V, the molecular ion (m/z = 40) nearly saturates the detector (limit on the signal is 1V). In the same spectrum, an argon cluster peak ($(Ar)_2^+$ at m/z = 80) is detected at S/N of $23\sigma$, which will be used to demonstrate the role of the new pulser. Originally, the target was the doubly ionized $Ar^{2+}$ (m/z = 20), however, during testing we found out that this peaks quickly saturates the detector, forcing the use of a peak with lower intensity.

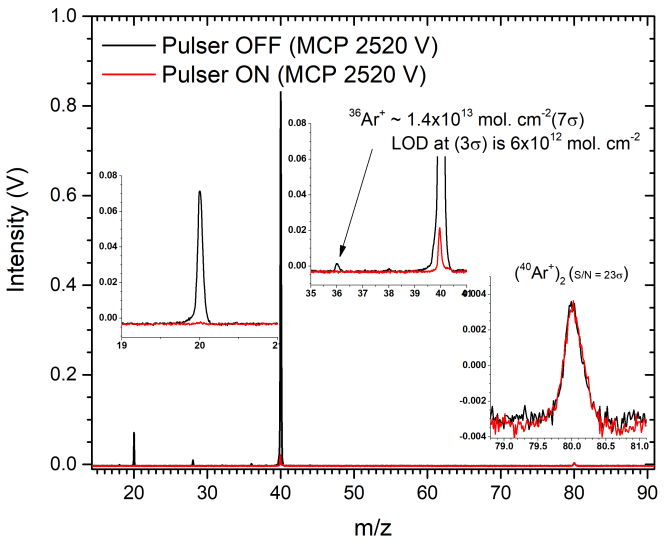


**Figure 2.10:** LDPI TOF MS of Argon ice at 20 K with a thickness of 17.5 ML with the pulser on and off at a low MCP value. The limit of detection (LoD) is calculated based on the natural abundance of $^{36}Ar$ at m/z = 36.

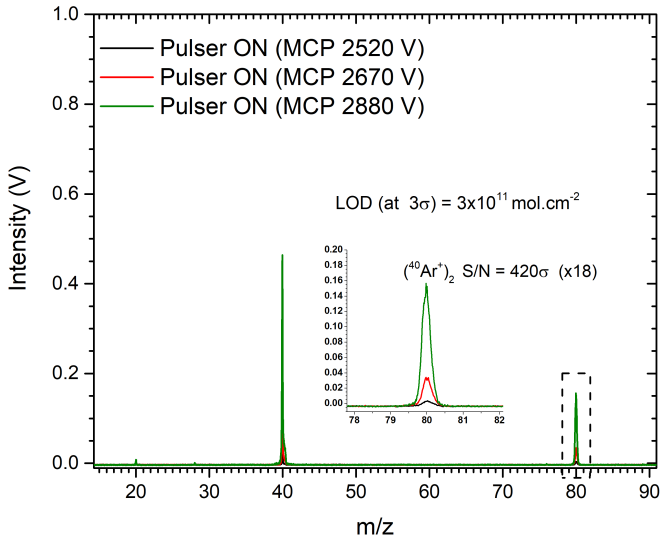


**Figure 2.11:** LDPI TOF MS of Argon ice at 20 K with a thickness of 17.5 ML with the pulser on allowing to increase the MCP value. The new limit of detection (LoD) is calculated based on an increase in the S/N of the $(Ar)_2^+$ mass peak at m/z = 80.

The pulser settings have been calibrated to deflect all ions including and below m/z = 40. This corresponds to a time delay setting of $\Delta t_2 = 1.95$ $\mu$s, with the voltage dip of 50 V, for 2 $\mu$s. It is shown in Fig. 2.10 ('Pulser ON' trace) that the pulser efficiently deflects (most) ions below the set threshold, and does not affect the measurement of $(Ar)_2^+$. This deflection window can be shorter, down to 0.2 $\mu$s, however, for the purpose of this test, it is kept wide. With the pulser deflecting the ions, the MCP voltage is increased in three steps and this corresponds to the S/N of the peak at m/z = 80, equal to 420, shown Fig. 2.11. In comparison the to the measurements with the pulser off, it as an improvement by a factor of 18. Under the assumption that the gain of the detector is similar in the mass range between m/z = 36 - 80, we estimate that the new LoD for MATRI$^2$ICES is equal to $3 \times 10^{11}$ molecules cm$^{-2}$.

## 2.6 Conclusion

MATRI$^2$ICES is an experimental system using Laser Desorption Post Ionization Time-of-Flight Mass Spectrometry to probe and quantify photon-triggered processes in interstellar ice analogues. In the field of astrochemistry this is a unique setup. In this section the setup has been described, along with the key calibration experiments and measuring techniques, proving its potential to investigate the VUV photolysis of interstellar ices.